



PCCP

**UV Photodissociation Dynamics of the Acetone Oxide  
Criegee Intermediate: Experiment and Theory**

Journal:	<i>Physical Chemistry Chemical Physics</i>
Manuscript ID	CP-ART-01-2023-000207.R1
Article Type:	Paper
Date Submitted by the Author:	10-Feb-2023
Complete List of Authors:	Wang, Guanghan; University of Pennsylvania, Chemistry Liu, Tianlin; University of Pennsylvania, Chemistry Department Zou, Meijun; University of Pennsylvania, Chemistry Karsili, Tolga; university of Louisiana at Lafayette, Chemistry Lester, Marsha; University of Pennsylvania, Department of Chemistry

SCHOLARONE™  
Manuscripts

# UV Photodissociation Dynamics of the Acetone Oxide Criegee Intermediate: Experiment and Theory

Guanghan Wang,<sup>1†</sup> Tianlin Liu,<sup>1†</sup> Meijun Zou,<sup>1</sup> Tolga N. V. Karsili,<sup>2,\*</sup> and Marsha I. Lester<sup>1,\*</sup>

<sup>1</sup> Department of Chemistry, University of Pennsylvania, Philadelphia, PA 19104-6323 USA

<sup>2</sup> Department of Chemistry, University of Louisiana at Lafayette, Lafayette, LA 70504 USA

## Abstract

The photodissociation dynamics of the dimethyl-substituted acetone oxide Criegee intermediate [(CH<sub>3</sub>)<sub>2</sub>COO] is characterized following electronic excitation to the bright <sup>1</sup>ππ\* state, which leads to O (<sup>1</sup>D) + acetone [(CH<sub>3</sub>)<sub>2</sub>CO, S<sub>0</sub>] products. The UV action spectrum of (CH<sub>3</sub>)<sub>2</sub>COO recorded with O (<sup>1</sup>D) detection under jet-cooled conditions is broad, unstructured, and essentially unchanged from the corresponding electronic absorption spectrum obtained using a UV-induced depletion method. This indicates that UV excitation of (CH<sub>3</sub>)<sub>2</sub>COO leads predominantly to the O (<sup>1</sup>D) product channel. A higher energy O (<sup>3</sup>P) + (CH<sub>3</sub>)<sub>2</sub>CO (T<sub>1</sub>) product channel is not observed, although it is energetically accessible. In addition, complementary MS-CASPT2 trajectory surface-hopping (TSH) simulations indicate minimal population leading to the O (<sup>3</sup>P) channel and non-unity overall probability for dissociation (within 100 fs). Velocity map imaging of the O (<sup>1</sup>D) products is utilized to reveal the total kinetic energy release (TKER) distribution upon photodissociation of (CH<sub>3</sub>)<sub>2</sub>COO at various UV excitation energies. Simulation of the TKER distributions is performed using a hybrid model that combines an impulsive model with a statistical component, the latter reflecting the longer-lived (> 100 fs) trajectories identified in the TSH calculations. The impulsive model accounts for vibrational activation of (CH<sub>3</sub>)<sub>2</sub>CO arising from geometrical changes between the Criegee intermediate and the carbonyl product, indicating the importance of CO stretch, CCO bend, and CC stretch along with activation of hindered rotation and rock of the methyl groups in the (CH<sub>3</sub>)<sub>2</sub>CO product. Detailed comparison is also made with the TKER distribution arising from photodissociation dynamics of CH<sub>2</sub>OO upon UV excitation.

---

<sup>†</sup> Equal contributions.

\* Corresponding author emails: [milester@sas.upenn.edu](mailto:milester@sas.upenn.edu), [tolga.karsili@louisiana.edu](mailto:tolga.karsili@louisiana.edu)

## 1. Introduction

Ozonolysis is a significant tropospheric removal pathway for alkenes, the most abundant non-methane volatile organic compounds emitted into the atmosphere, which originate from biogenic and anthropogenic sources.<sup>1-4</sup> Alkene ozonolysis proceeds by cycloaddition of ozone across the C=C double bond to form a primary ozonide, which fragments into carbonyl and zwitterionic carbonyl oxide products, the latter known as the Criegee intermediate.<sup>5</sup> The Criegee intermediates are initially formed with high internal energy and undergo rapid unimolecular decay or collisional stabilization. Thermalization is followed by unimolecular decay and/or bimolecular reaction with atmospheric species such as water vapor, formic acid, and SO<sub>2</sub>.<sup>6,7</sup> Unimolecular decay of Criegee intermediates is an important source of OH radicals,<sup>8-11</sup> thereby impacting the oxidative capacity of the atmosphere. Bimolecular reactions of Criegee intermediates are implicated in the formation of secondary organic aerosols.<sup>12, 13</sup>

Ozonolysis of alkenes with terminal methylene, ethylidene or isopropylidene groups yield the simplest formaldehyde oxide [CH<sub>2</sub>OO], methyl-substituted acetaldehyde oxide [CH<sub>3</sub>CHOO, *syn* or *anti*], or dimethyl-substituted acetone oxide [(CH<sub>3</sub>)<sub>2</sub>COO] Criegee intermediates, respectively.<sup>14, 15</sup> The *syn* and *anti* conformers of CH<sub>3</sub>CHOO (relative stabilities of 0.0 and 3.6 kcal mol<sup>-1</sup>) are oriented with the methyl group pointing toward or away from the terminal oxygen, respectively.<sup>16</sup> The two conformers are separated by a high isomerization barrier of ca. 35 kcal mol<sup>-1</sup> and are typically treated as distinct species.<sup>15</sup>

Thus far, experimental and theoretical studies have investigated the electronic spectroscopy of a broad range of Criegee intermediates,<sup>16-39</sup> in each case revealing a strong S<sub>2</sub>←S<sub>0</sub> transition to an excited <sup>1</sup>ππ\* state primarily associated with the carbonyl oxide moiety. Upon electronic excitation, the Criegee intermediates are predicted to access a repulsive region of the S<sub>2</sub> state and undergo rapid dissociation to O-atom and carbonyl co-products. For CH<sub>2</sub>OO, CH<sub>3</sub>CHOO, and (CH<sub>3</sub>)<sub>2</sub>COO, the co-products are formaldehyde [H<sub>2</sub>CO], acetaldehyde [CH<sub>3</sub>CHO], and acetone [(CH<sub>3</sub>)<sub>2</sub>CO], respectively.<sup>16, 27, 28, 40-45</sup>

The photodissociation dynamics of CH<sub>2</sub>OO and CH<sub>3</sub>CHOO have been characterized under jet-cooled conditions by UV action spectroscopy and velocity map imaging (VMI), in both cases with O-atom detection.<sup>40-43</sup> The experimental studies and associated theory showed that UV-induced photodissociation leads to two spin-allowed product channels, specifically a lower energy channel to singlet products, O (<sup>1</sup>D) + co-product (S<sub>0</sub>), and a higher energy channel to triplet products, O (<sup>3</sup>P) + co-product (T<sub>1</sub>).<sup>16, 27, 28, 40-45</sup> The distinct product channels were probed independently by 2+1 resonance-enhanced multiphoton ionization (REMPI) of the O (<sup>1</sup>D) or O (<sup>3</sup>P<sub>2</sub>) products at 205.47 nm or 225.66 nm.<sup>46, 47</sup>

For CH<sub>2</sub>OO, VMI experiments yielded broad total kinetic energy release (TKER) distributions for both the O (<sup>1</sup>D) and O (<sup>3</sup>P) product channels.<sup>40, 41, 43</sup> The termination of the TKER distribution obtained for the O (<sup>3</sup>P) + H<sub>2</sub>CO (T<sub>1</sub>) channel was utilized to determine the asymptotic dissociation energy at ca. 76 kcal mol<sup>-1</sup> (3.3 eV), corresponding to a threshold excitation wavelength of 378 nm.<sup>41</sup> The asymptotic

dissociation energy for the lower energy O ( $^1\text{D}$ ) + H<sub>2</sub>CO (S<sub>0</sub>) product channel was then derived at ca. 49 kcal mol<sup>-1</sup> (2.1 eV) by accounting for the well-known singlet-triplet splittings of the O-atom (1.97 eV)<sup>48</sup> and H<sub>2</sub>CO products (3.12 eV).<sup>40,41</sup> In addition, UV action spectra were obtained by stepping the UV excitation across the S<sub>2</sub>←S<sub>0</sub> transition with O ( $^1\text{D}$ ) or O ( $^3\text{P}$ ) product detection, noting that the O ( $^3\text{P}$ ) + H<sub>2</sub>CO (T<sub>1</sub>) product channel turned on gradually above its energetic threshold.<sup>41,42</sup>

Recently, analysis of VMI results obtained at  $\lambda \leq 350$  nm revealed a bimodal TKER distribution in the measured O ( $^1\text{D}$ ) signal where an unexpected low TKER component was observed, corresponding to highly internally excited H<sub>2</sub>CO (S<sub>0</sub>) products. In the same study, trajectory surface hopping (TSH) calculations<sup>44</sup> using the “on-the-fly” energies and forces computed using the complete active space self-consistent field (CASSCF) method attributed the two TKER components of CH<sub>2</sub>OO to different dynamical pathways. The population prepared in the S<sub>2</sub> state can couple to other singlet states (S<sub>0</sub>, S<sub>1</sub>, S<sub>3</sub>, S<sub>4</sub>, S<sub>5</sub>, S<sub>6</sub>) via conical intersections (CoIn) that lead to dissociation. In particular, population initially evolving on the S<sub>5</sub> or S<sub>6</sub> states en route to forming O ( $^3\text{P}$ ) + H<sub>2</sub>CO (T<sub>1</sub>) products may undergo internal conversion to the S<sub>3</sub> or S<sub>4</sub> states at the second conical intersection (CoIn2) to form O ( $^1\text{D}$ ) + H<sub>2</sub>CO (S<sub>0</sub>) products. The H<sub>2</sub>CO (S<sub>0</sub>) products formed this way would be generated with high internal excitation, corresponding to the low energy component in the TKER distributions of the O ( $^1\text{D}$ ) products.<sup>44</sup>

Later, a full-dimensional TSH study<sup>49</sup> on CH<sub>2</sub>OO with “on-the-fly” energies and forces calculated at the higher-level multi-state complete active space with second-order perturbation theory (MS-CASPT2) method predicted prompt dissociation within 50 fs with a unity quantum yield upon vertical excitation to the bright S<sub>2</sub> state. Analysis of the trajectories revealed an 80:20 branching into the O ( $^1\text{D}$ ) or O ( $^3\text{P}$ ) product channel and a long-range internal conversion from the S<sub>5</sub> or S<sub>6</sub> to the S<sub>0</sub>, S<sub>1</sub>, S<sub>2</sub>, S<sub>3</sub>, or S<sub>4</sub> states at asymptotic O-O separations.<sup>49</sup> This TSH study suggested that the low TKER component may arise via internal conversion at classically asymptotic O-O bond distances, driven by motion in the HCO bend and CO stretch vibrations of the H<sub>2</sub>CO partner.

Similarly, both O ( $^1\text{D}$ ) and O ( $^3\text{P}$ ) product channels were observed following electronic excitation of CH<sub>3</sub>CHOO to the  $^1\pi\pi^*$  state.<sup>42</sup> The termination of the associated TKER distributions obtained by VMI again yielded asymptotic dissociation energy limits of ca. 55.9 and 88.3 kcal mol<sup>-1</sup> for the two product channels. This study focused on the more stable *syn* conformer of CH<sub>3</sub>CHOO, which has a stronger absorption than *anti*-CH<sub>3</sub>CHOO at the higher energies / shorter wavelengths (e.g. 305 nm) utilized to determine the product asymptotes.<sup>23,24,50-52</sup> Moreover, the O ( $^1\text{D}$ ) action spectrum of CH<sub>3</sub>CHOO mirrored the electronic absorption spectrum obtained under jet-cooled conditions, indicating the dominant O ( $^1\text{D}$ ) + CH<sub>3</sub>CHO (S<sub>0</sub>) product channel.<sup>42</sup> By contrast, the O ( $^3\text{P}$ ) action spectrum of CH<sub>3</sub>CHOO exhibited a gradual onset above the energetic threshold for O ( $^3\text{P}$ ) + CH<sub>3</sub>CHO (T<sub>1</sub>) products, which occurs near the peak of the absorption spectrum.<sup>42</sup>

This study provides the first experimental and theoretical examination of the photodissociation dynamics of the  $(\text{CH}_3)_2\text{COO}$  Criegee intermediate upon excitation to the  $\text{S}_2$  state. Although two spin-allowed product channels are energetically accessible, only the lower-energy  $\text{O} (^1\text{D}) + (\text{CH}_3)_2\text{CO} (\text{S}_0)$  product channel is experimentally observed using UV action spectroscopy and VMI. The resultant experimental TKER distributions are simulated using an impulsive model, revealing significant internal excitation of the acetone products. Complementary CASPT2 calculations are utilized to compute the potential energy profiles of the lowest seven electronic states along the O-O stretch coordinate. High level trajectory surface hopping calculations are performed to interpret the dissociation dynamics. Finally, the UV photodissociation dynamics of  $(\text{CH}_3)_2\text{COO}$  are compared with prior studies of  $\text{CH}_2\text{OO}$  and to a limited extent *syn*- $\text{CH}_3\text{CHOO}$ , providing new insights on the photochemistry of these prototypical Criegee intermediates.

## 2. Methods

### 2.1 Experimental

In this study, the UV photodissociation dynamics of  $(\text{CH}_3)_2\text{COO}$  is investigated through two types of experiments: UV action spectroscopy and velocity map imaging. In both cases,  $\text{O} (^1\text{D})$  products are detected by 2+1 REMPI at 205 nm.<sup>47</sup> In the first type of experiment, an UV action spectrum for  $(\text{CH}_3)_2\text{COO}$  is recorded by scanning the UV excitation wavelength over the 280 to 370 nm range in 1-3 nm steps. Analogous experiments were conducted with detection of  $\text{O} (^3\text{P}_{2,1,0})$  by 2+1 REMPI at ca. 226 nm.<sup>53,54</sup> The  $\text{O} (^3\text{P}_j)$  background signal arising from photolysis of  $\text{O}_2$  by the 226 nm laser was removed using a background subtraction scheme as in prior studies.<sup>41,42</sup> In the second type of experiment, VMI measurements are conducted to obtain the velocity and angular distributions of the  $\text{O} (^1\text{D})$  products following UV excitation of  $(\text{CH}_3)_2\text{COO}$  at discrete UV wavelengths in the 295-330 nm region.

Synthesis of the 2,2-diodopropane [ $(\text{CH}_3)_2\text{CI}_2$ ] precursor and the generation of the  $(\text{CH}_3)_2\text{COO}$  Criegee intermediate have been described previously.<sup>25</sup> In brief, the vapor of  $(\text{CH}_3)_2\text{CI}_2$  is entrained in 20%  $\text{O}_2/\text{Ar}$  carrier gas (10 psi) and pulsed through a nozzle (Parker-Hannifin General Valve Series 9, 1 mm orifice) into a quartz capillary tube reactor (1 mm I.D., ~25 mm length) at 10 Hz. The precursor is photolyzed by 248 nm radiation using a KrF excimer laser (Coherent, COMPex 102) near the exit of the capillary reactor tube, producing a monoiodo alkyl radical, which subsequently reacts with  $\text{O}_2$  to generate the Criegee intermediate. The Criegee intermediates are then collisionally stabilized in the capillary and jet-cooled in the ensuing supersonic expansion.

Approximately 4 cm downstream, after passing through a skimmer (2 mm diameter, Beam Dynamics) into a laser interaction region, the Criegee intermediates are crossed by the UV ‘pump’ radiation (280-370 nm,  $< 0.12 \text{ cm}^{-1}$  linewidth), which is generated by frequency doubling the output of a dye laser (Radiant

Dyes, NarrowScan) pumped by the second harmonic output of a Nd:YAG laser (InnoLas, SpitLight 600). After a short time delay ( $\sim 50$  ns), the resultant O ( $^1D$ ) products are ionized by the counter-propagating UV ‘probe’ laser via 2+1 REMPI.<sup>47</sup> The probe laser radiation is generated by frequency tripling the output of another dye laser (Continuum, ND6000, R640) pumped by the second harmonic output of a Nd:YAG laser (Continuum, Powerlite 8010). The probe radiation is focused (40 cm f.l.) and spatially overlapped with the focused pump radiation (30 cm f.l.). The polarizations of the pump and probe radiation are both set parallel to the detector plane. The wavelength (vacuum) is calibrated with a high-resolution wavemeter (Coherent WaveMaster), and the power is measured with a power meter (Gentec TPM-300).

The generated ions are velocity-mapped onto a spatially and temporally sensitive multi-channel plate (MCP)/phosphor screen coupled detector, which is temporally gated for the O<sup>+</sup> ( $m/z$  16) mass channel. The central region of the detector is protected using a physical beam block of 3 mm diameter, which prevents the ions of low translational energy ( $\leq 200$  cm<sup>-1</sup>) from striking the detector.<sup>41, 42</sup> In VMI measurements, the 2D spatial images are captured by a CCD camera and analyzed using the pBASEX inversion method to extract the velocity and angular distribution of the O ( $^1D$ ) products,<sup>55</sup> resulting in an energy resolution ( $\Delta E/E$ ) of  $\sim 10\%$ . The radial distributions are obtained by integrating over the angular coordinate of the images, providing the velocity distribution of the O ( $^1D$ ) products. The total kinetic energy release distributions are then derived using conservation of linear momentum. The probe laser is scanned over the O-atom Doppler profile ( $\pm 0.3$  cm<sup>-1</sup>) during the image collection.

Background O ( $^1D$ ) signal primarily originates from IO, which is a common byproduct in the generation of Criegee intermediates.<sup>17, 18, 56</sup> Photolysis of IO by the probe laser yields I\* ( $^2P_{1/2}$ ) and background O ( $^1D$ ),<sup>57</sup> the latter of which is also ionized by the probe laser. As a result, a background subtraction scheme is applied in both types of experiments by operating the pump and probe laser at 5 Hz and 10 Hz, respectively, to subtract the O ( $^1D$ ) signal arising from the IO byproduct. In addition, the IO photodissociation process has been well-studied and is used to calibrate the VMI setup.<sup>41-43</sup>

## 2.2 Theoretical

In this study, the ground state minimum energy geometry and normal mode wavenumbers were calculated at the B2PLYP-D3/cc-pVTZ level of theory as implemented in Gaussian 16.<sup>58</sup> This method has been shown to perform well in determining geometries and normal mode wavenumbers of Criegee intermediates.<sup>30, 35, 38, 49, 59</sup>

Vertical excitation energies (VEE) of CH<sub>2</sub>OO, *syn*-CH<sub>3</sub>CHOO and (CH<sub>3</sub>)<sub>2</sub>COO to their lowest six singlet electronically excited states are calculated using the complete active space with second-order perturbation theory (CASPT2) with the aug-cc-pVTZ basis set.<sup>60-63</sup> The CASPT2 calculations are based

on a 14-state-averaged complete active space self-consistent field (SA14-CASSCF) reference wavefunction, involving the lowest seven singlet states and seven triplet states. An active space consisting of 10 electrons and 8 orbitals was employed. The molecular orbitals used for the three Criegee intermediates are depicted in Figure S1. An imaginary level shift of 0.5 Hartree is applied to every CASPT2 calculation to aid convergence and mitigate the involvement of intruder states.

Next, the energies required for the spin-allowed dissociation to the lower energy O ( $^1D$ ) + co-product ( $S_0$ ) channel and the higher energy O ( $^3P$ ) + co-product ( $T_1$ ) channel for  $CH_2OO$ , *syn*- $CH_3CHOO$ , and  $(CH_3)_2COO$  are evaluated. For the lower energy product asymptote of each Criegee intermediate, a constrained ground state geometry optimization was performed at large O-O separation (fixed at 4.0 Å) using the B2PLYP-D3/cc-pVTZ level of theory. The COO angle is fixed at the ground state equilibrium geometry value of the respective Criegee intermediate to facilitate convergence. The returned geometry is then used to compute single-point CASPT2 energies using the same active space and basis set as described above. In addition, the ground state equilibrium geometry of each aldehyde/ketone ( $S_0$ ) alone is optimized as well to compare with the geometry of the corresponding dissociation co-product obtained with a distant O-atom, showing no structural differences (Table S1). Then the dissociation energies for the lower energy product channel are derived by taking the CASPT2 energy difference between the O ( $^1D$ ) + co-product ( $S_0$ ) and the parent Criegee intermediate. For each co-product, a geometry optimization and single-point energy calculation was also carried out at its lowest triplet state ( $T_1$ ) at the B2PLYP-D3/cc-pVTZ level of theory to evaluate the  $S_0$ - $T_1$  energy splitting. The dissociation energies for the higher energy product channel are derived by combining the dissociation energies for the lower energy product channel with the  $S_0$ - $T_1$  splitting for the co-products and the well-known singlet-triplet splitting for the O-atom (1.97 eV).<sup>48</sup> Anharmonic zero-point energy (ZPE) corrections are included for each Criegee intermediate and the corresponding aldehyde/ketone co-product ( $S_0$  and  $T_1$ ) when evaluating the O-O bond dissociation energies.

Unrelaxed (rigid-body) potential energy curves for the lowest seven singlet electronic states of  $(CH_3)_2COO$  are evaluated along the O-O bond stretch coordinate ( $R_{OO}$ ) using the CASPT2/aug-cc-pVDZ level of theory. This calculation is carried out by elongating the O-O bond distance while freezing the remainder of the nuclear coordinates at the ground state minimum geometry of  $(CH_3)_2COO$ . The potential energy curves for  $CH_2OO$  and *syn*- $CH_3CHOO$  have been reported previously using the same rigid-body bond scan method and level of theory.<sup>45</sup>

Trajectory surface hopping (TSH) simulations were performed on  $(CH_3)_2COO$  using Newton-X.<sup>64, 65</sup> Initial positions and momenta were obtained by sampling the ground state phase space using a Wigner distribution based on the B2PLYP-D3/cc-pVTZ equilibrium geometry and associated harmonic normal mode wavenumbers of  $(CH_3)_2COO$ . In the TSH simulations, the nuclear coordinates were propagated by

integrating Newton's classical equations using the velocity Verlet algorithm in steps of 0.5 fs, while the electronic coordinates were propagated by numerically solving the time-dependent Schrödinger equation using Butcher's fifth-order Runge-Kutta method in steps of 0.025 fs.<sup>66,67</sup> Trajectories were initiated on the  $S_2$  state, and the energies and gradients of the seven lowest singlet states were calculated "on-the-fly" using the single-state, single-reference CASPT2(10,8)/cc-pVDZ (SS-SR-CASPT2) method.<sup>68</sup> SS-SR-CASPT2 enables the computation of energies and analytical gradients at MS-CASPT2 quality, at a reduced computational cost; it also performs well near electronic state degeneracies. The state hopping probabilities were evaluated by calculating the non-adiabatic coupling matrix elements at the SS-SR-CASPT2 level. A total of 99 trajectories for  $(\text{CH}_3)_2\text{COO}$  were propagated in this study.

The CASPT2 energies for the TSH simulations were performed via the BAGEL, which interfaces with Newton-X,<sup>69</sup> while the rest of the CASPT2 calculations were performed using MOLPRO v2020.1.<sup>70-72</sup> The Gaussian and MOLPRO calculations were performed utilizing XSEDE resources.<sup>73</sup>

### 3. Results

#### 3.1 Potential Energy Profiles

The vertical excitation energies and associated oscillator strengths ( $f$ ) to the lowest six singlet excited electronic states of  $\text{CH}_2\text{OO}$ , *syn*- $\text{CH}_3\text{CHOO}$ , and  $(\text{CH}_3)_2\text{COO}$  have been investigated previously at various level of theories.<sup>21,31</sup> In this study, the VEEs for  $(\text{CH}_3)_2\text{COO}$  are re-evaluated using the CASPT2(10,8)/aug-cc-pVTZ method at their ground state minimum energy geometries, along with those computed for  $\text{CH}_2\text{OO}$  and *syn*- $\text{CH}_3\text{CHOO}$  using the same method for direct comparison (Tables 1 and S2). For each Criegee intermediate, only the  $S_1$  and  $S_2$  states are energetically accessible upon near-UV excitation. Electronic excitation to the  $S_1$  state of each Criegee intermediate involves a  $\pi^* \leftarrow n$  transition with poor spatial overlap between the participating orbitals and negligible oscillator strength. By contrast, the  $S_2$  state is of  ${}^1\pi\pi^*$  character with the participating orbitals showing good spatial overlap, which results in a large oscillator strength.<sup>45</sup> As a result, the UV excitation of these Criegee intermediates is expected to exclusively populate the bright  $S_2$  state. The VEEs evaluated in this study for the  $S_2 \leftarrow S_0$  transitions of the three Criegee intermediate agree well with previous calculations<sup>21,31</sup> and the peak positions of the electronic absorption spectra obtained experimentally (Table 1).<sup>16-18,23-27</sup>

UV excitation of the  $(\text{CH}_3)_2\text{COO}$  is expected to result in O-O bond fission, as found for other Criegee intermediates.<sup>34,35,38-41,43,44,52,74</sup> Here, a rigid-body scan is performed for  $(\text{CH}_3)_2\text{COO}$  along the O-O stretch coordinate ( $R_{\text{OO}}$ ), analogous to prior studies.<sup>44,45</sup>

Table 1. Computed vertical excitation energies and experimental peak absorption under jet-cooled conditions for  $(\text{CH}_3)_2\text{COO}$ , *syn*- $\text{CH}_3\text{CHOO}$ , and  $\text{CH}_2\text{OO}$ . Zero-point corrected product asymptotic energies for the two spin-allowed product channels and zero-point corrected  $S_0$ - $T_1$  energy splittings of the acetone [ $(\text{CH}_3)_2\text{CO}$ ], acetaldehyde [ $\text{CH}_3\text{CHO}$ ] and formaldehyde [ $\text{H}_2\text{CO}$ ] products. Experimental values reported in the literature are listed in brackets.

Criegee Intermediate	VEE ( $S_2 \leftarrow S_0$ ) eV (nm)	Peak Absorption eV (nm)	O ( $^1\text{D}$ ) + co-product ( $S_0$ ) eV (kcal mol $^{-1}$ )	O ( $^3\text{P}$ ) + co-product ( $T_1$ ) eV (kcal mol $^{-1}$ )	co-product $S_0$ - $T_1$ splitting eV (kcal mol $^{-1}$ )
$(\text{CH}_3)_2\text{COO}$	3.97 (312)	[3.84 (323)] <sup>a</sup>	2.35 (54.1)	3.79 (87.4)	3.41 (78.7) [3.5 (81)] <sup>f</sup>
<i>syn</i> - $\text{CH}_3\text{CHOO}$	3.98 (312)	[3.87 (320)] <sup>b</sup>	2.33 (53.8)	3.65 (84.3)	3.29 (75.9) [3.38 (77.9)] <sup>g</sup>
$\text{CH}_2\text{OO}$	3.87 (320)	[3.70 (335)] <sup>c</sup>	2.26 (52.2)	3.32 (76.5)	3.02 (69.7) [3.13 (72.1)] <sup>h</sup>

<sup>a</sup> Ref. 25. <sup>b</sup> Ref. 16. <sup>c</sup> Ref. 27. <sup>d</sup> Ref. 42. <sup>e</sup> Ref. 41. <sup>f</sup> Ref. 75. <sup>g</sup> Ref. 76. <sup>h</sup> Ref. 77.

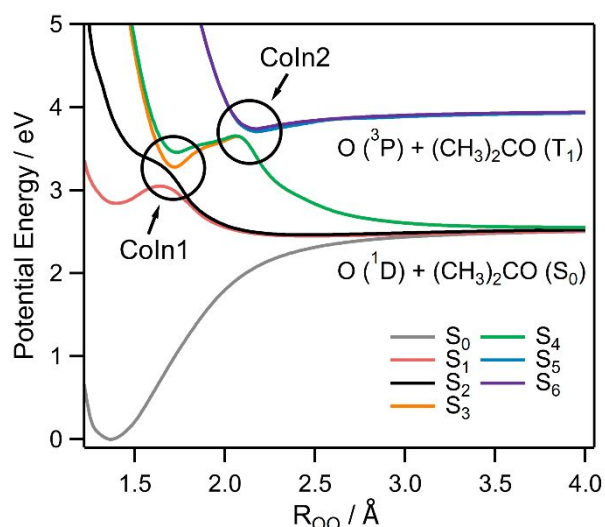


Figure 1. Adiabatic potential energy curves (unrelaxed) computed along the O-O bond dissociation coordinate for the lowest seven singlet states of  $(\text{CH}_3)_2\text{COO}$ . The lower five states ( $S_0$ ,  $S_1$ ,  $S_2$ ,  $S_3$ ,  $S_4$ ) lead to the O ( $^1\text{D}$ ) +  $(\text{CH}_3)_2\text{CO}$  ( $S_0$ ) asymptote, while the higher two states ( $S_5$ ,  $S_6$ ) lead to the O ( $^3\text{P}$ ) +  $(\text{CH}_3)_2\text{CO}$  ( $T_1$ ) asymptote. Calculations are conducted at the CASPT2(10,8)/aug-cc-pVDZ level of theory. CoIn1 and CoIn2 indicate the two conical intersections.

As displayed in Figure 1, the ground state ( $S_0$ ) of  $(\text{CH}_3)_2\text{COO}$  is bound with respect to  $R_{\text{OO}}$  and correlates to the lowest energy spin-allowed asymptote that forms O ( $^1\text{D}$ ) +  $(\text{CH}_3)_2\text{CO}$  ( $S_0$ ). The  $S_1$  and  $S_2$  states are quasi-bound with respect to  $R_{\text{OO}}$ , both correlating adiabatically to the lowest energy asymptote and diabatically to the higher energy O ( $^3\text{P}$ ) +  $(\text{CH}_3)_2\text{CO}$  ( $T_1$ ) asymptotic products. The  $S_1$  and  $S_2$  states encounter a conical intersection (CoIn1) with the  $S_3$  and  $S_4$  states at  $R_{\text{OO}} \sim 1.7$  Å. A second conical intersection (CoIn2) occurs at  $R_{\text{OO}} \sim 2.1$  Å between the  $S_3$ ,  $S_4$ ,  $S_5$  and  $S_6$  states. Following electronic

excitation to the  $S_2$  state, the population can either traverse around the CoIn1 region and continue along the adiabatic  $S_2$  surface to form the lowest energy products, or pass through the CoIn1 and undergo internal conversion to the higher  $S_3$  or  $S_4$  states. In the latter case, the evolving population on the  $S_3$  or  $S_4$  states will encounter CoIn2. Again, traversing around or passing through CoIn2 may lead to the lower or higher energy products, respectively. As a result, internal conversion to higher singlet electronic states ( $S_5$  and/or  $S_6$ ) is required to form the higher energy products. Thus, the branching into the two product asymptotes is affected by the relative energy of the product asymptotes as well as the non-adiabatic coupling strength at (and around) CoIn1 and CoIn2.

Next, the computed energies for the lower energy  $O(^1D) + \text{co-product}$  ( $S_0$ ) asymptotes and the  $S_0-T_1$  spacing of the co-products, along with the well-known singlet-triplet splitting of the O-atom (1.97 eV),<sup>48</sup> are combined to derive the higher energy  $O(^3P) + \text{co-product}$  ( $T_1$ ) asymptotes. The computed  $S_0-T_1$  spacing of the co-products are in good accord (within 0.1 eV) with prior experimental studies for  $H_2CO$ ,<sup>77</sup>  $CH_3CHO$ ,<sup>76</sup> and  $(CH_3)_2CO$ .<sup>75</sup> In addition, the computed asymptotic energies for *syn*- $CH_3CHOO$  and  $CH_2OO$  agree well with prior experimental reports (within 0.2 eV).<sup>41,42</sup> The computed energies are compiled in Table 1, along with available experimental values for comparison. For  $(CH_3)_2COO$ , the computed asymptotic energies are 2.35 eV or 3.79 eV, corresponding to UV excitation wavelength of 528 nm or 327 nm.

### 3.2 UV Action Spectrum

Previously, the electronic absorption spectrum of jet-cooled  $(CH_3)_2COO$  was recorded by measuring the UV-induced depletion of the VUV (10.5 eV) photoionization signal at  $m/z$  74, which is shown in Figure 2.<sup>25</sup> The absorption spectrum peaks at ca. 323 nm with the full-width at half-maximum (FWHM) of ca. 35 nm derived from a Gaussian fit.<sup>25</sup> The absorption spectrum was attributed to the strong  $S_2 \leftarrow S_0$  transition of  $(CH_3)_2COO$  induced by UV excitation, which results in dissociation to O-atom and acetone products.

In this study, we recorded the UV action spectrum of jet-cooled  $(CH_3)_2COO$  by stepping the UV excitation wavelength across a broad spectral range of 280-370 nm, while selectively detecting the O ( $^1D$ ) products using 2+1 REMPI and monitoring the  $O^+$  signal induced by UV excitation. The resultant O ( $^1D$ ) action spectrum of  $(CH_3)_2COO$  is remarkably similar to the previously observed absorption spectrum under jet-cooled conditions (Figure 2), with error bars indicative of standard deviations ( $\pm 1\sigma$ ) derived from repeated measurements. It is also in good accord, although slightly narrower, than the previously reported direct absorption spectrum obtained under thermal conditions by Huang et al. (Figure S2).<sup>78</sup> A Gaussian fit is used to represent the action spectrum, yielding the peak position at ca. 323 nm and FWHM of ca. 40 nm, which is consistent with the previously reported absorption spectrum. The similarity of the

spectral profiles suggests that UV excitation of  $(\text{CH}_3)_2\text{COO}$  to the  $S_2$  state predominantly leads to  $\text{O} (^1\text{D}) + (\text{CH}_3)_2\text{CO} (S_0)$  products.

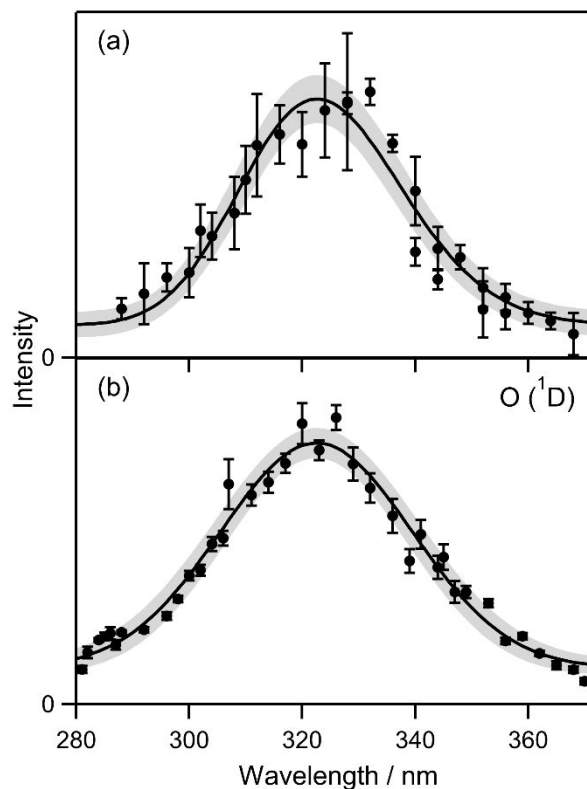


Figure 2. (a) Previously reported UV absorption spectrum for  $(\text{CH}_3)_2\text{COO}$  under jet-cooled condition. (b) UV action spectrum of  $(\text{CH}_3)_2\text{COO}$  recorded under similar conditions with  $\text{O} (^1\text{D})$  detection by 2+1 REMPI. The error bars represent the standard deviation ( $\pm 1\sigma$ ) derived from repeated measurements. In each case, the experimental data is well represented as a Gaussian function with uncertainty indicated by the shaded region. The data in panel (a) is adapted with permission from Ref. 25.

Earlier studies reported UV action spectra of  $\text{CH}_2\text{OO}$  and *syn*- $\text{CH}_3\text{CHOO}$  with detection of  $\text{O} (^1\text{D})$  and  $\text{O} (^3\text{P})$  products associated with the two dissociation asymptotes.<sup>40-42</sup> In these systems, a gradual onset of  $\text{O} (^3\text{P})$  products was observed at UV excitation energies above the higher energy product asymptote.<sup>41, 42</sup> However,  $\text{O} (^3\text{P})$  products are not detected upon excitation of  $(\text{CH}_3)_2\text{COO}$  at or above photon energies corresponding to the energetic limit for forming  $\text{O} (^3\text{P}) + (\text{CH}_3)_2\text{CO} (T_1)$  products. This suggests that alternative pathways redirect population to the lower energy  $\text{O} (^1\text{D}) + (\text{CH}_3)_2\text{CO} (S_0)$  product asymptote or, more generally, other pathways remove population from electronically excited states of  $(\text{CH}_3)_2\text{COO}$ . As a result, we carry out complementary TSH calculations (Sec. 3.4) to investigate the photodissociation dynamics of  $(\text{CH}_3)_2\text{COO}$ .

### 3.3 Velocity Map Imaging Studies

The photodissociation dynamics of the  $(\text{CH}_3)_2\text{COO}$  Criegee intermediate is probed using VMI, which involves UV excitation of  $(\text{CH}_3)_2\text{COO}$  followed by 2+1 REMPI probing of nascent O ( $^1\text{D}$ ) products to obtain the angular and radial distributions of the O ( $^1\text{D}$ ) products. The O ( $^1\text{D}$ ) velocity map images are recorded at four discrete UV wavelengths in the 295-330 nm region and are displayed in Figures 3 and S2. The angular distributions of the O ( $^1\text{D}$ ) products are anisotropic ( $\beta \sim 0.9$ -1.0 (0.2)); see Table S3) and consistent with the computed transition dipole moment vector relative to the O-O bond axis (see Scheme S1). The anisotropic angular distributions indicate that dissociation of  $(\text{CH}_3)_2\text{COO}$  is rapid compared to its rotational period (ca. 200 ps).

A representative TKER distribution of the O ( $^1\text{D}$ ) products arising from excitation of  $(\text{CH}_3)_2\text{COO}$  at 295 nm is shown in Figure 3, while results at other wavelengths are given in Figure S3. The TKER distribution is unstructured and exhibits slight asymmetry toward higher energy. An average TKER ( $\langle \text{TKER} \rangle$ ) of  $2840 \text{ cm}^{-1}$  and FWHM of  $3150 \text{ cm}^{-1}$  are obtained upon excitation at 295 nm.

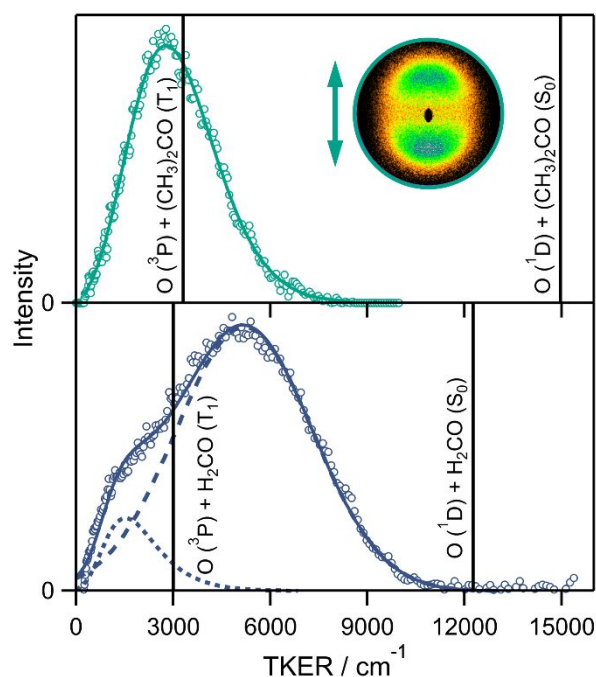


Figure 3. Total kinetic energy release distributions obtained by velocity map imaging of the O ( $^1\text{D}$ ) products following UV excitation of (top)  $(\text{CH}_3)_2\text{COO}$  at 295 nm and (bottom)  $\text{CH}_2\text{OO}$  at 340 nm. The TKER distribution in the top panel is fit to a polynomial function (solid) to guide the eye. The TKER distributions in the bottom panel is well represented with a bimodal Gaussian-Gumbel distribution (solid), where the two components are denoted by dashed (Gaussian) and dotted (Gumbel) lines. The inset shows the raw image of the O ( $^1\text{D}$ ) products from photodissociation of  $(\text{CH}_3)_2\text{COO}$ , with a double-sided arrow representing the polarization of the UV radiation. The vertical lines in each panel indicate the calculated energy available ( $E_{\text{avl}}$ ) to the O ( $^1\text{D}$ ) + co-product ( $\text{S}_0$ ) or O ( $^3\text{P}$ ) + co-product ( $\text{T}_1$ ). The  $\text{CH}_2\text{OO}$  TKER distribution is adapted with permission from Ref. 44.

Applying conservation of energy, the energy available ( $E_{\text{avl}}$ ) to the products at each UV excitation wavelength is evaluated as follows

$$E_{\text{avl}} = h\nu - D = \text{TKER} + E_{\text{int}}$$

where  $h\nu$  is the UV photon energy and  $D$  is the bond dissociation energy required to form the O ( $^1\text{D}$ ) +  $(\text{CH}_3)_2\text{CO}$  ( $\text{S}_0$ ) products. The internal energy of  $(\text{CH}_3)_2\text{CO}$  is assumed to be negligible under jet-cooled conditions.  $E_{\text{avl}}$  is partitioned into kinetic energy of recoiling fragments (TKER) and internal excitation of  $(\text{CH}_3)_2\text{CO}$  ( $\text{S}_0$ ) products ( $E_{\text{int}}$ ). The energy available to O ( $^1\text{D}$ ) +  $(\text{CH}_3)_2\text{CO}$  ( $\text{S}_0$ ) products increases from approximately 11400 to 15000  $\text{cm}^{-1}$  over the UV range examined (330-295 nm). However, the TKER distribution remains almost unchanged with  $\langle\text{TKER}\rangle$  of ca. 2900  $\text{cm}^{-1}$  and FWHM of ca. 2900  $\text{cm}^{-1}$  (Table S3). The similarity of the TKER distributions is notable given that the range of excitation wavelengths results in ca. 3600  $\text{cm}^{-1}$  change in energy available to products. The net result is a higher degree of internal excitation of the  $(\text{CH}_3)_2\text{CO}$  products, increasing from 74% to 81% of the available energy as the Criegee intermediate is excited with increasing UV excitation energy.

By contrast, a prior VMI study of  $\text{CH}_2\text{OO}$  exhibited a bimodal TKER distribution for the O ( $^1\text{D}$ ) +  $\text{H}_2\text{CO}$  ( $\text{S}_0$ ) products at UV excitation wavelengths shorter than 350 nm, as shown in Figure 3.<sup>44</sup> A bimodal TKER distribution was also observed for the O ( $^1\text{D}$ ) product channel resulting from photodissociation of *syn*- $\text{CH}_3\text{CHOO}$  at  $\lambda \leq 320$  nm.<sup>42</sup> However, a bimodal TKER distribution is not observed for the O ( $^1\text{D}$ ) product channel of  $(\text{CH}_3)_2\text{COO}$  over the range of strongly absorbing UV wavelengths examined here. A more detailed comparison of the TKER distributions for these Criegee intermediates will be addressed later (Sec. 4.2 and 4.3).

### 3.4 Trajectory Calculations

TSH studies are performed to simulate the photodissociation dynamics of  $(\text{CH}_3)_2\text{COO}$  following excitation to the bright  $\text{S}_2$  state in order to interpret the experimental results. Figure 4 presents the time evolution of the normalized population in the lowest seven singlet electronic states, namely  $\text{S}_0$ ,  $\text{S}_1$ ,  $\text{S}_2$ ,  $\text{S}_3$ ,  $\text{S}_4$ ,  $\text{S}_5$ , and  $\text{S}_6$ , of  $(\text{CH}_3)_2\text{COO}$  (left) and  $\text{CH}_2\text{OO}$  (right, reproduced from Ref. 49). The excited  $\text{S}_2$  state of  $(\text{CH}_3)_2\text{COO}$  begins to depopulate at ca. 10 fs, followed by initial internal conversion to the  $\text{S}_1$  state in ca. 10-20 fs, and then to the  $\text{S}_0$ ,  $\text{S}_3$  and  $\text{S}_4$  states in ca. 15-25 fs. Further internal conversion to the  $\text{S}_5$  and  $\text{S}_6$  states occurs after ca. 25 fs. At 100 fs, the TSH results indicate that ca. 10% of the total population is in the  $\text{S}_5$  and  $\text{S}_6$  states, which are the only states that correlate with the higher energy O ( $^3\text{P}$ ) +  $(\text{CH}_3)_2\text{CO}$  ( $\text{T}_1$ ) product asymptote (see Figure 1). By comparison, internal conversion starting from the  $\text{S}_2$  state of  $\text{CH}_2\text{OO}$  to the other singlet states is predicted to be relatively faster and result in a two-fold larger percentage of population in the combined  $\text{S}_5$  and  $\text{S}_6$  states at long time (ca. 20% of total).<sup>49</sup>

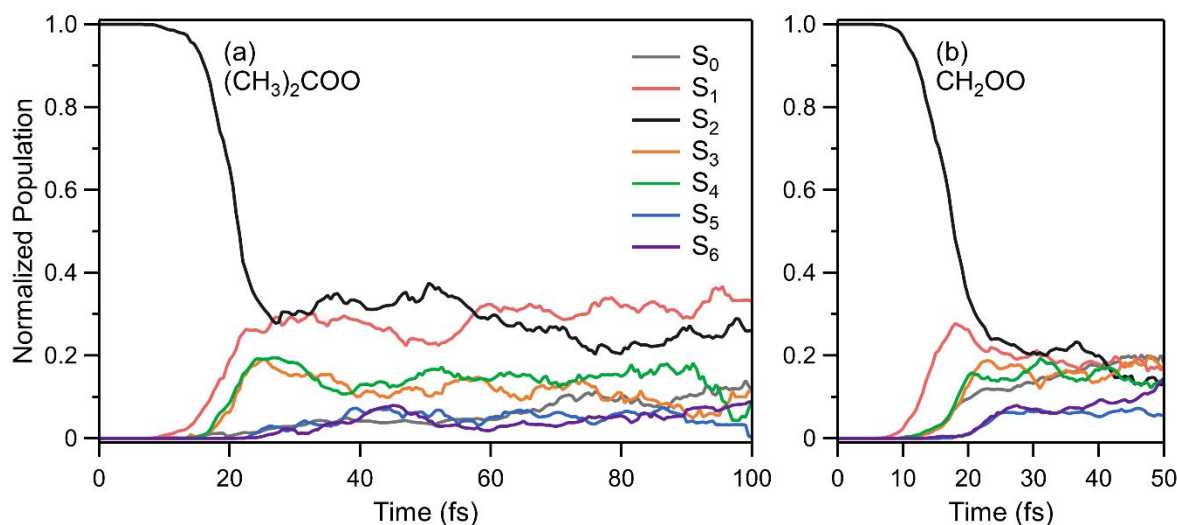


Figure 4. Normalized population as a function of time (fs) along the lowest seven singlet states for (a)  $(\text{CH}_3)_2\text{COO}$  and (b)  $\text{CH}_2\text{OO}$ . The  $\text{CH}_2\text{OO}$  TSH results are reproduced with permission from Ref. 49.

For  $\text{CH}_2\text{OO}$ , all of the trajectories undergo prompt O-O bond fission within 50 fs with unity quantum yield as shown by the individual (gray) and average (red) trajectory profiles in Figure 5. Moreover, population in the  $S_5$  or  $S_6$  states of  $\text{CH}_2\text{OO}$  readily dissociates to form  $\text{O} (^3\text{P}) + \text{H}_2\text{CO} (\text{T}_1)$  products.

By contrast, dissociation of  $(\text{CH}_3)_2\text{COO}$  occurs more slowly and is incomplete within 100 fs as shown by the individual (gray) trajectories in Figure 5. Here, a  $R_{\text{OO}}$  value of  $2.5 \text{ \AA}$ , where the lower five and upper two electronic states become nearly degenerate, is considered as the geometric threshold for dissociation. Among the 99 trajectories for  $(\text{CH}_3)_2\text{COO}$ , 71 exhibit direct O-O dissociation similar to that seen for  $\text{CH}_2\text{OO}$ , but with a relatively slower dissociation rate than  $\text{CH}_2\text{OO}$ .<sup>49</sup> Another 19 trajectories show a partial oscillation in the O-O coordinate prior to dissociation. The remaining 9 trajectories continue to oscillate in the O-O coordinate throughout the trajectory and do not dissociate within 100 fs. These trends are readily seen by averaging the trajectories at each  $R_{\text{OO}}$  step that exhibit similar behavior: the yellow trace represents those that undergo direct dissociation, the green trace illustrates temporary trapping in the O-O coordinate prior to dissociation, and the purple trace shows long-lived behavior with continued oscillation in the O-O coordinate for at least 100 fs. The long-lived trajectories exhibit a ca. 50 fs period of oscillation, corresponding to a ca.  $700 \text{ cm}^{-1}$  vibrational frequency, which suggests an extended O-O bond length. These long-lived trajectories remain as the parent  $(\text{CH}_3)_2\text{COO}$  molecule. They may further relax within the  $S_2$  state, internally convert and relax in the  $S_1$  state, or eventually dissociate on a longer time scale. As a result, the TSH calculations predict fewer trajectories leading to dissociation upon  $S_2 \leftarrow S_0$  vertical excitation of the  $(\text{CH}_3)_2\text{COO}$  Criegee intermediate, corresponding to a non-unity quantum yield. Compared to  $\text{CH}_2\text{OO}$ , a smaller fraction of  $(\text{CH}_3)_2\text{COO}$  undergo dissociation

and a smaller portion of these lead to the  $S_5$  and  $S_6$  states, which correlate with  $O(^3P) + (CH_3)_2CO(T_1)$  products, consistent with the lack of  $O(^3P)$  products observed experimentally.

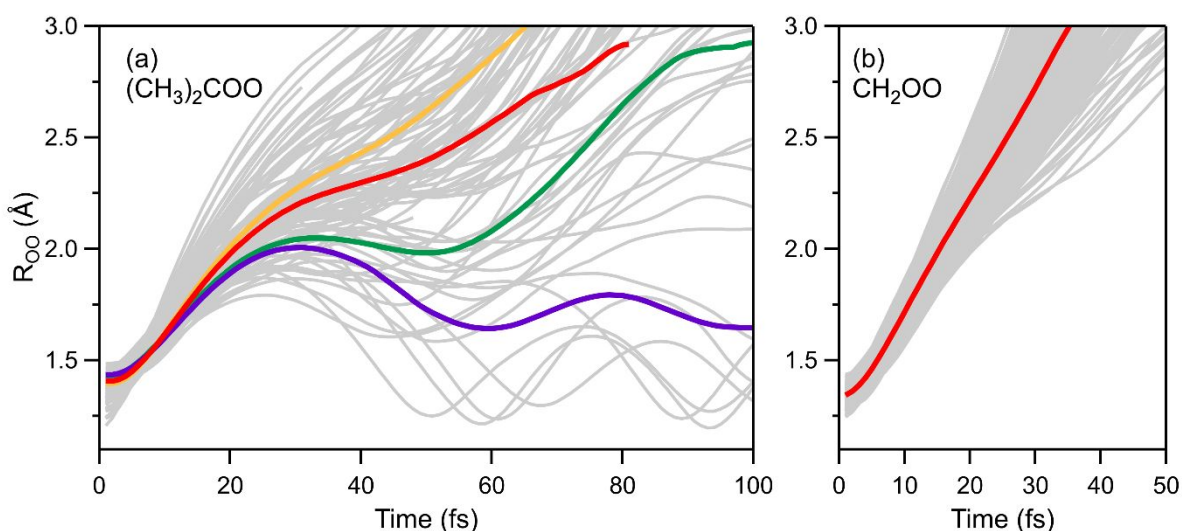


Figure 5. Variation of the O-O bond distance ( $R_{OO}$ ) following  $S_2 \leftarrow S_0$  vertical excitation of (a)  $(CH_3)_2COO$  and (b)  $CH_2OO$  as a function of time. Each trajectory is shown as a gray line and the red line is the average  $R_{OO}$  of all trajectories at each time step. In panel (a), the yellow line shows the average  $R_{OO}$  for the traces that are directly dissociative, the green line represents the average of those that become temporarily trapped in the O-O coordinate prior to dissociation, and the purple line corresponds to the average of those trajectories that do not dissociate within 100 fs. The  $CH_2OO$  trajectories are reproduced with permission from Ref. 49.

## 4. Discussion

### 4.1 $O(^3P)$ product channels

The ground state minimum energy geometries of  $(CH_3)_2COO$ , *syn*- $CH_3CHOO$ , and  $CH_2OO$  are of  $C_s$  symmetry with the heavy atoms in a common plane (Figure S4). For the former two, a weak intramolecular interaction between two H-atoms of the methyl substituent and the terminal oxygen stabilizes the  $\pi$ -orbital of the ground state ( $S_0$ ) and destabilizes the  $\pi^*$ -orbital of the  $S_2$  state, thus increasing the  $S_2$ - $S_0$  energy gap. This is observed experimentally as a shift in the peak absorption for  $(CH_3)_2COO$  and  $CH_3CHOO$  towards higher energy (shorter wavelength) by ca. 0.2 eV ( $\Delta\lambda \sim 15$  nm) compared to  $CH_2OO$  (Table 1).<sup>16-18, 23-27</sup> This is consistent with the VEE computed for the  $S_2 \leftarrow S_0$  transitions of  $(CH_3)_2COO$  (3.97 eV, 312 nm) and *syn*- $CH_3CHOO$  (3.98 eV, 312 nm), which are slightly higher than that for  $CH_2OO$  (3.87 eV, 320 nm) (see Table 1).

As shown in Figure 6 and Table 1, the dissociation energies computed for the lower  $O(^1D) +$  co-product ( $S_0$ ) channels of the three Criegee intermediates are similar within 0.1 eV. However, the  $S_0 - T_1$  energy gap progressively increases from formaldehyde < acetaldehyde < acetone, manifesting in an increase by ca. 0.3 eV in the dissociation energies for forming  $O(^3P) +$  co-product ( $T_1$ ) from  $CH_2OO$  to

*syn*-CH<sub>3</sub>CHO and a further increase by ca. 0.2 eV from *syn*-CH<sub>3</sub>CHO to (CH<sub>3</sub>)<sub>2</sub>COO. Accordingly, the calculated energetic threshold for forming the O (<sup>3</sup>P) + co-product (T<sub>1</sub>) shifts towards much higher energy from CH<sub>2</sub>OO to (CH<sub>3</sub>)<sub>2</sub>COO by 0.5 eV, which is greater than the shift in the VEE (0.1 eV). Experimentally, the onset of the O (<sup>3</sup>P) action spectrum shifted from 365 nm (3.40 eV) for CH<sub>2</sub>OO to 324 nm (3.83 eV) for *syn*-CH<sub>3</sub>CHO, a change of ca. 0.4 eV, while the corresponding spectral peak shifted from 335 nm (3.70 eV) for CH<sub>2</sub>OO to 320 nm (3.87 eV) for *syn*-CH<sub>3</sub>CHO, a change of ca. 0.2 eV, consistent with calculations.<sup>16, 27, 41, 42</sup> The spectral peak of (CH<sub>3</sub>)<sub>2</sub>COO was observed at 323 nm (3.84 eV), which is close to that of *syn*-CH<sub>3</sub>CHO. However, the further increase of ca. 0.2 eV between the S<sub>0</sub> and T<sub>1</sub> product states from *syn*-CH<sub>3</sub>CHO to (CH<sub>3</sub>)<sub>2</sub>COO results in an anticipated onset of the O (<sup>3</sup>P) action spectrum for (CH<sub>3</sub>)<sub>2</sub>COO at shorter wavelength than *syn*-CH<sub>3</sub>CHO, where a gradual onset of the O (<sup>3</sup>P) + CH<sub>3</sub>CHO (T<sub>1</sub>) product channel occurred near the peak of the absorption spectrum.<sup>42</sup>

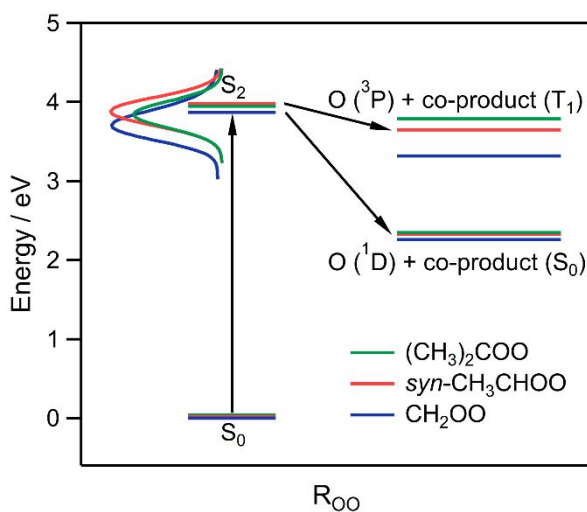


Figure 6. Schematic diagram of spin-allowed product asymptotes following vertical S<sub>2</sub>←S<sub>0</sub> excitation of (CH<sub>3</sub>)<sub>2</sub>COO, *syn*-CH<sub>3</sub>CHO and CH<sub>2</sub>OO. The left column shows the absorption spectra (Gaussian fits) obtained previously under jet-cooled conditions (adapted with permission from Ref. 25). The right column shows the O (<sup>1</sup>D) + co-product (S<sub>0</sub>) (lower) and O (<sup>3</sup>P) + co-product (T<sub>1</sub>) (higher) spin-allowed product channels. The computed vertical excitation energies and asymptotic dissociation energies are listed in Table 1.

In this study, the potential energy curves of (CH<sub>3</sub>)<sub>2</sub>COO are computed using the same method as those of CH<sub>2</sub>OO and *syn*-CH<sub>3</sub>CHO reported previously,<sup>44, 45, 49</sup> enabling a direct comparison of the three Criegee intermediates. From CH<sub>2</sub>OO to (CH<sub>3</sub>)<sub>2</sub>COO, a significant increase of the energy splittings between the lowest two spin-allowed dissociation asymptotes results in a steeper slope between the two CoIn regions. Therefore, population traversing through CoIn1 experiences an unfavorable “uphill” motion in order to reach the higher energy O (<sup>3</sup>P) + co-product (T<sub>1</sub>) asymptote. In particular, TSH calculations predict 10% of the (CH<sub>3</sub>)<sub>2</sub>COO population on the S<sub>5</sub> and S<sub>6</sub> states combined at long time scales, which is two-fold less than that of CH<sub>2</sub>OO.<sup>49</sup> Moreover, a substantial number of (CH<sub>3</sub>)<sub>2</sub>COO

trajectories exhibit oscillations about the Franck-Condon region of the  $S_2$  or  $S_1$  state, rather than undergo prompt dissociation as for  $\text{CH}_2\text{OO}$ , leading to a non-unity quantum yield for O-O bond fission.

To summarize, we attribute the absence of the O ( $^3\text{P}$ ) products from the photodissociation experiments of  $(\text{CH}_3)_2\text{COO}$  to a combination of factors, including a gradual onset of the O ( $^3\text{P}$ ) +  $(\text{CH}_3)_2\text{CO}$  ( $T_1$ ) product channel above its energetic threshold, which is shifted to higher energy compared to  $\text{CH}_2\text{OO}$  and *syn*- $\text{CH}_3\text{CHOO}$ ,<sup>41, 42</sup> its less populated  $S_5$  and/or  $S_6$  states and/or lower overall probability for dissociation.

## 4.2 Impulsive Model

This laboratory recently developed a reduced impulsive model to interpret the experimental TKER distributions obtained upon photodissociation of a series of four-carbon unsaturated Criegee intermediates, which provided new insight on vibrational activation of the carbonyl products.<sup>39</sup> In this work, the reduced impulsive model is utilized to simulate the TKER distribution resulting from photodissociation of  $\text{CH}_2\text{OO}$ , while a hybrid version of the model combining impulsive and statistical components is utilized for  $(\text{CH}_3)_2\text{COO}$ . In brief, the reduced impulsive model assumes that the available energy is partitioned into a subset of vibrational modes of the carbonyl product and translational energy of the recoiling fragments. The vibration modes excited are those associated with significant geometric changes in the carbonyl product ( $S_0$ ) compared to the equilibrium geometry of Criegee intermediate ( $S_0$ ).

For  $\text{CH}_2\text{OO}$ , geometric changes in the  $\text{H}_2\text{CO}$  ( $S_0$ ) product suggest that five in-plane vibrational modes will be excited, namely CO stretch,  $\text{CH}_2$  symmetric stretch,  $\text{CH}_2$  asymmetric stretch  $\text{CH}_2$  scissor, and CO wag (Figure S5). These modes reflect the significant changes in CO and CH bond lengths and HCO angles around the carbon-atom (Table S4). The remaining  $\text{CH}_2$  out-of-plane wag is unlikely to be excited due to lack of an out-of-plane force during O-O bond fission.<sup>45</sup> In addition, the TSH results for  $\text{CH}_2\text{OO}$  (Figure 5) show that all trajectories undergo prompt O-O bond fission within 50 fs, supporting the direct dissociation assumption required for the reduced impulsive model.

The reduced impulsive model then assumes that all energetically allowed vibrational states involving these vibrational modes are populated equally.<sup>39</sup> The density of translational states is expressed as  $\rho(E_T) = A_T(E_{\text{avl}} - E_{\text{int}})^{1/2}$ , where  $E_T$  is the translational energy constrained by conservation of energy ( $E_T = E_{\text{avl}} - E_{\text{int}}$ ) and  $A_T$  is a normalization factor. Building on prior work,<sup>40, 41</sup> an impulsive model for rotational partitioning<sup>79</sup> is used to estimate rotational excitation of  $\text{H}_2\text{CO}$ , which predicts  $E_{\text{rot}} = 0.20 E_T$ . Along with the experimentally derived dissociation energy (Table 1), the simulated translational energy distribution is obtained by summing over all vibrational states and taking into account the experimental resolution ( $\Delta E/E \sim 10\%$ ). For  $\text{CH}_2\text{OO}$ , the reduced impulsive model yields a TKER distribution that is in good accord with experiment, as shown in Figure 7; however, the simulated TKER distribution exhibits

oscillations (ca. 1300  $\text{cm}^{-1}$  spacing likely due to CO wag) as a result of the low density of  $\text{H}_2\text{CO}$  vibrational states. Nevertheless, the reduced impulsive model captures the main properties of the experimental TKER distribution.

For  $(\text{CH}_3)_2\text{COO}$ , the reduced impulsive model indicates that nine vibrational modes of the  $(\text{CH}_3)_2\text{CO}$  product (Figure S5) are likely to be excited by comparing the equilibrium ground-state geometry of  $(\text{CH}_3)_2\text{COO}$  with that of the  $(\text{CH}_3)_2\text{CO}$  product (Table S4). Specifically, the CO double bond is compressed by 0.06 Å from  $(\text{CH}_3)_2\text{COO}$  to  $(\text{CH}_3)_2\text{CO}$ , and the bond angles that involve the carbonyl group with the methyl substituent on either the opposite or same side, denoted as *anti*- or *syn*-methyl, are enlarged by 5.8° or 3.0°, respectively. Combined with the extension by 0.03 or 0.04 Å in either CC bond, we anticipate that CO stretch, two CCO bends, and two CC stretches will be vibrationally excited in the  $(\text{CH}_3)_2\text{CO}$  products. In addition, the weak intramolecular interaction between H-atoms of the *syn*-methyl substituent and the terminal oxygen in  $(\text{CH}_3)_2\text{COO}$  results in a ca. 60° rotation of the methyl group compared to its orientation in  $(\text{CH}_3)_2\text{CO}$  product, as illustrated by the Newman projections in Figure S4. Upon photodissociation of  $(\text{CH}_3)_2\text{COO}$ , significant hindered rotational excitation of these methyl groups is expected, along with vibrational activation of the methyl in-plane rock (Figure S5). Overall rotational excitation of the  $(\text{CH}_3)_2\text{CO}$  product is neglected, as the torque imparted by O-O bond fission is expected to primarily result in vibrational activation of bending motions that involve the carbonyl group.

For photodissociation of  $(\text{CH}_3)_2\text{COO}$  at 320 nm, the reduced impulsive model predicts a broader and more highly excited TKER distribution than observed experimentally. As a result, we investigated an alternative hybrid model that combines the impulsive model with a statistical component, the latter reflecting the longer-lived (> 100 fs) trajectories identified in the TSH calculations for  $(\text{CH}_3)_2\text{COO}$  (Figure 5). We anticipate that the statistical component arises from intramolecular vibrational energy redistribution occurring on a ps timescale.<sup>80</sup> A statistical component accounting for ca. 20% of the available energy brings the simulated TKER distribution into good accord with experiment, as shown in Figure 7. Further exploration indicates that the statistical component increases from ca. 15 to 35% upon excitation of  $(\text{CH}_3)_2\text{COO}$  from 330 to 295 nm. The resultant simulated TKER distributions are essentially unchanged with excitation energy, consistent with the experimental distributions (Figure S6).

In Figure 7, the experimental TKER distribution obtained upon photodissociation of  $(\text{CH}_3)_2\text{COO}$  at 320 nm is compared with that for  $\text{CH}_2\text{OO}$  at 340 nm, where the energy available ( $E_{\text{avl}}$ ) to the O ( $^1\text{D}$ ) + co-product ( $\text{S}_0$ ) is similar (ca. 12300  $\text{cm}^{-1}$ ). A significantly lower average TKER and narrower FWHM of the distribution is found for  $(\text{CH}_3)_2\text{COO}$  compared to the corresponding parameters for  $\text{CH}_2\text{OO}$  by ca. 50%. These changes in the TKER distributions reflect the different degree of vibrational excitation in the carbonyl co-products upon photodissociation, which primarily originates from activation of the hindered rotational modes associated with the methyl substituents. In addition, because the methyl substituents are

15 times heavier than hydrogen atoms, the stretching and bending modes involving the methyl substituents are significantly lower in frequency (by ca. 65%), leading to a higher density of  $(\text{CH}_3)_2\text{CO}$  product vibrational states that can accommodate the available energy compared to that for  $\text{H}_2\text{CO}$ .

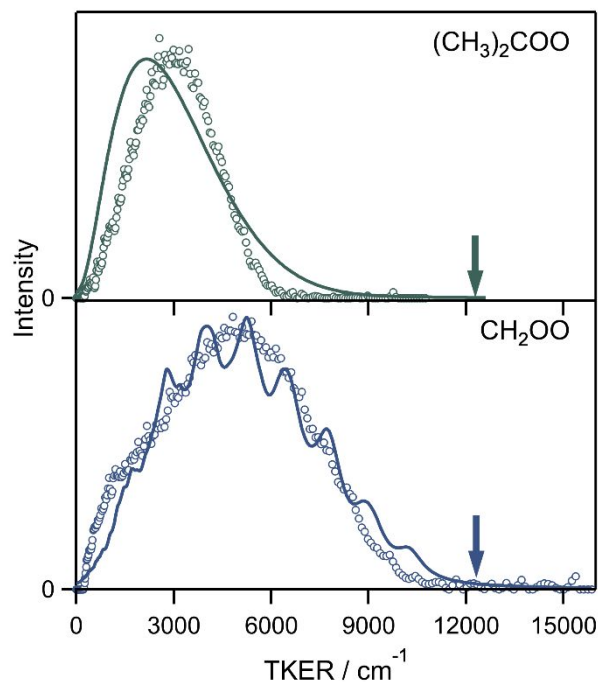


Figure 7. Simulated translational energy distributions for  $\text{O} (^1\text{D}) + \text{co-products}$  upon photodissociation of  $(\text{CH}_3)_2\text{COO}$  and  $\text{CH}_2\text{OO}$  (solid lines) using reduced impulsive models with and without a statistical component, respectively. Also shown for comparison are experimental TKER distributions (open circles) obtained by velocity map imaging of  $\text{O} (^1\text{D})$  products following UV excitation of  $(\text{CH}_3)_2\text{COO}$  at 320 nm and  $\text{CH}_2\text{OO}$  at 340 nm. The energy available to products in each case is ca. 12300  $\text{cm}^{-1}$  and indicated with an arrow. The experimental data for  $\text{CH}_2\text{OO}$  is adapted with permission from Ref. 44.

### 4.3 Low TKER component in $\text{O} (^1\text{D})$ product channels

Previously, analysis of VMI results obtained for  $\text{CH}_2\text{OO}$  at UV excitation wavelengths below 350 nm revealed a bimodal TKER distribution for the  $\text{O} (^1\text{D}) + \text{H}_2\text{CO} (\text{S}_0)$  product channel, where an unexpected low TKER component associated with highly internally excited  $\text{H}_2\text{CO} (\text{S}_0)$  products was identified.<sup>44</sup> For example, the TKER distribution obtained at 340 nm is reproduced in Figure 3 with the high and low TKER components denoted as the dashed and dotted lines, respectively. The low TKER component accounts for ca. 10% of the total  $\text{O} (^1\text{D})$  product yield by area (Table S3). A similar, but weaker, low TKER shoulder was reported previously upon photodissociation of *syn*- $\text{CH}_3\text{CHOO}$  at 305 and 320 nm.<sup>42</sup>

A recent full-dimensional TSH study using the MS-CASPT2 method proposed a long-range internal conversion mechanism, which may account for the low TKER component associated with the highly internally excited  $\text{H}_2\text{CO} (\text{S}_0)$  products upon photodissociation of  $\text{CH}_2\text{OO}$ .<sup>49</sup> This mechanism involved a portion of the population approaching the higher energy  $\text{O} (^3\text{P}) + \text{H}_2\text{CO} (\text{T}_1)$  product asymptote ( $\text{S}_5$  and

$S_6$ ) undergoing spin-allowed internal conversion at large O-O separation to form the lower energy O ( $^1D$ ) +  $H_2CO$  ( $S_0$ ) products.<sup>49</sup> From an energetic perspective, this mechanism requires the UV excitation energy to be above the O ( $^3P$ ) product asymptote of  $CH_2OO$  (3.28 eV or 378 nm), consistent with the longest UV wavelength of 350 nm that yields a clearly evident low TKER component.

By comparison, no distinguishable low TKER feature is discerned upon excitation of  $(CH_3)_2COO$  at 295 nm (Figure 3). Although the UV excitation energy is higher than the O ( $^3P$ ) +  $(CH_3)_2CO$  ( $T_1$ ) product asymptote, an analogous internal conversion pathway does not appear to be available for  $(CH_3)_2COO$ . This is consistent with the lack of detectable O ( $^3P$ ) products.

## 5. Conclusions

The photodissociation dynamics of the dimethyl-substituted acetone oxide Criegee intermediate [ $(CH_3)_2COO$ ] is investigated experimentally and theoretically following UV excitation on the strong  $S_2 \leftarrow S_0$  transition of  $^1\pi\pi^*$  character, along with comparisons to  $CH_2OO$  and *syn*- $CH_3CHOO$  in multiple aspects. Theory predicts two spin-allowed dissociation limits for each Criegee intermediate, namely a lower energy O ( $^1D$ ) + co-product ( $S_0$ ) and a higher energy O ( $^3P$ ) + co-product ( $T_1$ ) channels. The VEE to the  $S_2$  state and the dissociation energies associated with the two product asymptotes are evaluated for each system, showing good agreement with prior experiments.<sup>16, 25, 27, 41, 42, 75-77</sup>

Surprisingly, O ( $^3P$ ) products are not experimentally detected following UV excitation of  $(CH_3)_2COO$  in this study, which likely originates from a combination of spectral and dynamical causes. We anticipate a gradual onset of the O ( $^3P$ ) product channel above its energetic threshold, which is shifted to higher energy for  $(CH_3)_2COO$  compared to *syn*- $CH_3CHOO$  and  $CH_2OO$ .<sup>41, 42</sup> Moreover, complementary trajectory calculations demonstrate a non-unity photodissociation yield, along with smaller population of the  $S_5$  and/or  $S_6$  states that lead to O ( $^3P$ ) products compared to those of  $CH_2OO$ .<sup>49</sup>

VMI experiments probing the O ( $^1D$ ) products from photodissociation of  $(CH_3)_2COO$  at discrete UV wavelengths yield broad and unstructured TKER distributions associated with highly internally excited  $(CH_3)_2CO$  ( $S_0$ ) products. A hybrid model that combines an impulsive model with a statistical component that comprises 15 to 35% of the available gives good agreement with the experimental TKER distributions obtained upon photodissociation of  $(CH_3)_2COO$  over a range of energies. This statistical component is aligned with the TSH results, in which ca. 20% of the trajectories are transiently trapped in the O-O coordinate prior to dissociation and another ca. 10% continue to oscillate in the O-O coordinate for at least 100 fs, allowing for energy randomization. By contrast,  $CH_2OO$  promptly dissociates within 50 fs, and its TKER distributions are well-reproduced with a reduced impulsive model. In addition, both the average and FWHM of the TKER distributions for  $(CH_3)_2COO$  are significantly smaller than those for  $CH_2OO$ . This is primarily attributed to activation of hindered rotation and in-plane rock of the methyl

groups in the  $(\text{CH}_3)_2\text{CO}$  products, originating from a  $60^\circ$  reorientation of the *syn*-methyl group compared to  $(\text{CH}_3)_2\text{COO}$ .

A low TKER component was previously observed in the O ( $^1\text{D}$ ) product channel of  $\text{CH}_2\text{OO}$  upon UV excitation at  $\lambda \leq 350$  nm,<sup>44</sup> and attributed to a long-range internal conversion mechanism as the products evolve toward the O ( $^3\text{P}$ ) asymptote.<sup>49</sup> By comparison, an analogous low TKER feature in the O ( $^1\text{D}$ ) product channel is not discerned for  $(\text{CH}_3)_2\text{COO}$  at energies where the O ( $^3\text{P}$ ) product channel is accessible, consistent with the absence of observed O ( $^3\text{P}$ ) products.

### Conflicts of Interest

There are no conflicts to declare.

### Acknowledgements

This research was supported by the U.S. Department of Energy - Basic Energy Sciences under grant DE-FG02-87ER13792 (MIL). This work utilized the Extreme Science and Engineering Discovery Environment (XSEDE) computer resources, which is supported by the National Science Foundation grant number ACI-1548562 through the allocation TG-CHE190088. Partial support of this research (TNVK) was provided by the National Science Foundation grant number CHE-2003422. Portions of this research were conducted with high performance computational resources provided by the Louisiana Optical Network Infrastructure (<http://www.loni.org>).

## References

1. D. Johnson and G. Marston, *Chem. Soc. Rev.*, 2008, **37**, 699-716.
2. C. A. Taatjes, D. E. Shallcross and C. J. Percival, *Phys. Chem. Chem. Phys.*, 2014, **16**, 1704-1718.
3. M. A. H. Khan, C. J. Percival, R. L. Caravan, C. A. Taatjes and D. E. Shallcross, *Environ. Sci.: Process. Impacts*, 2018, **20**, 437-453.
4. K. Sindelarova, C. Granier, I. Bouarar, A. Guenther, S. Tilmes, T. Stavrakou, J. F. Müller, U. Kuhn, P. Stefani and W. Knorr, *Atmos. Chem. Phys.*, 2014, **14**, 9317-9341.
5. R. Criegee, *Angew. Chem. Int. Ed.*, 1975, **14**, 745-752.
6. L. Vereecken, H. Harder and A. Novelli, *Phys. Chem. Chem. Phys.*, 2012, **14**, 14682-14695.
7. J. M. Anglada, J. Gonzalez and M. Torrent-Sucarrat, *Phys. Chem. Chem. Phys.*, 2011, **13**, 13034-13045.
8. L. Vereecken and J. S. Francisco, *Chem. Soc. Rev.*, 2012, **41**, 6259-6293.
9. T. A. Stephenson and M. I. Lester, *Int. Rev. Phys. Chem.*, 2020, **39**, 1-33.
10. M. I. Lester and S. J. Klippenstein, *Acc. Chem. Res.*, 2018, **51**, 978-985.
11. K. Riedel and K. Lassey, *Water. Atmos.*, 2008, **16**, 22-23.
12. C. J. Percival, O. Welz, A. J. Eskola, J. D. Savee, D. L. Osborn, D. O. Topping, D. Lowe, S. R. Utembe, A. Bacak, G. M. c Figgans, M. C. Cooke, P. Xiao, A. T. Archibald, M. E. Jenkin, R. G. Derwent, I. Riipinen, D. W. K. Mok, E. P. F. Lee, J. M. Dyke, C. A. Taatjes and D. E. Shallcross, *Faraday Discuss.*, 2013, **165**, 45-73.
13. R. Chhantyal-Pun, B. Rotavera, M. R. McGillen, M. A. H. Khan, A. J. Eskola, R. L. Caravan, L. Blacker, D. P. Tew, D. L. Osborn, C. J. Percival, C. A. Taatjes, D. E. Shallcross and A. J. Orr-Ewing, *ACS Earth Space Chem.*, 2018, **2**, 833-842.
14. R. A. Cox, M. Ammann, J. N. Crowley, H. Herrmann, M. E. Jenkin, V. F. McNeill, A. Mellouki, J. Troe and T. J. Wallington, *Atmos. Chem. Phys.*, 2020, **20**, 13497-13519.
15. L. Vereecken, A. Novelli and D. Taraborrelli, *Phys. Chem. Chem. Phys.*, 2017, **19**, 31599-31612.
16. J. M. Beames, F. Liu, L. Lu and M. I. Lester, *J. Chem. Phys.*, 2013, **138**, 244307.
17. L. Sheps, *J. Phys. Chem. L*, 2013, **4**, 4201-4205.
18. W.-L. Ting, Y.-H. Chen, W. Chao, M. C. Smith and J. J.-M. Lin, *Phys. Chem. Chem. Phys.*, 2014, **16**, 10438-10443.
19. E. S. Foreman, K. M. Kapnas, Y. Jou, J. Kalinowski, D. Feng, R. B. Gerber and C. Murray, *Phys. Chem. Chem. Phys.*, 2015, **17**, 32539-32546.
20. R. Dawes, B. Jiang and H. Guo, *J. Am. Chem. Soc.*, 2015, **137**, 50-53.
21. S. Srsen, D. Hollas and P. Slavicek, *Phys. Chem. Chem. Phys.*, 2018, **20**, 6421-6430.
22. J. Kalinowski, E. S. Foreman, K. M. Kapnas, C. Murray, M. Rasanen and R. B. Gerber, *Phys. Chem. Chem. Phys.*, 2016, **18**, 10941-10946.
23. M. C. Smith, W.-L. Ting, C.-H. Chang, K. Takahashi, K. A. Boering and J. J.-M. Lin, *J. Chem. Phys.*, 2014, **141**, 074302.
24. L. Sheps, A. M. Scully and K. Au, *Phys. Chem. Chem. Phys.*, 2014, **16**, 26701-26706.
25. F. Liu, J. M. Beames, A. M. Green and M. I. Lester, *J. Phys. Chem. A*, 2014, **118**, 2298-2306.
26. Y.-P. Chang, C.-H. Chang, K. Takahashi and J. J.-M. Lin, *Chem. Phys. Lett.*, 2016, **653**, 155-160.
27. J. M. Beames, F. Liu, L. Lu and M. I. Lester, *J. Am. Chem. Soc.*, 2012, **134**, 20045-20048.
28. P. Aplincourt, E. Henon, F. Bohr and M. F. Ruiz-López, *Chem. Phys.*, 2002, **285**, 221-231.
29. T. Liu, M. Zou, A. Caracciolo, C. A. Sojda and M. I. Lester, *J. Phys. Chem. A*, 2022, **126**, 6734-6741.
30. J. C. McCoy, B. Marchetti, M. Thodika and T. N. V. Karsili, *J. Phys. Chem. A*, 2021, **125**, 4089-4097.
31. K. Takahashi, *J. Phys. Chem. A*, 2022, **126**, 6080-6090.
32. B. Nikoobakht and H. Köppel, *Mol. Phys.*, 2021, **119**, 12433-12441.
33. B. Nikoobakht and H. Köppel, *Phys. Chem. Chem. Phys.*, 2022, **24**, 12433-12441.

34. M. F. Vansco, B. Marchetti and M. I. Lester, *J. Chem. Phys.*, 2018, **149**, 244309.
35. M. F. Vansco, B. Marchetti, N. Trongsrirawat, G. Wang, T. Bhagde, P. J. Walsh, S. J. Klippenstein and M. I. Lester, *J. Am. Chem. Soc.*, 2019, **141**, 15058-15069.
36. R. L. Caravan, M. F. Vansco, K. Au, M. A. H. Khan, Y.-L. Li, F. A. F. Winiberg, K. Zuraski, Y.-H. Lin, W. Chao, N. Trongsrirawat, P. J. Walsh, D. L. Osborn, C. J. Percival, J. J.-M. Lin, D. E. Shallcross, L. Sheps, S. J. Klippenstein, C. A. Taatjes and M. I. Lester, *Proc. Natl. Acad. Sci.*, 2020, **117**, 9733-9740.
37. Y.-H. Lin, C. Yin, K. Takahashi and J. J.-M. Lin, *Commun. Chem.*, 2021, **4**, 12.
38. G. Wang, T. Liu, A. Caracciolo, M. F. Vansco, N. Trongsrirawat, P. J. Walsh, B. Marchetti, T. N. V. Karsili and M. I. Lester, *J. Chem. Phys.*, 2021, **155**, 174305.
39. G. Wang, T. Liu, M. Zou, C. A. Sojidak, M. C. Kozlowski, T. N. V. Karsili and M. I. Lester, *J. Phys. Chem. A*, 2023, **127**, 203-215.
40. J. H. Lehman, H. Li, J. M. Beames and M. I. Lester, *J. Chem. Phys.*, 2013, **139**, 141103.
41. H. Li, Y. Fang, J. M. Beames and M. I. Lester, *J. Chem. Phys.*, 2015, **142**, 214312.
42. H. Li, Y. Fang, N. M. Kidwell, J. M. Beames and M. I. Lester, *J. Phys. Chem. A*, 2015, **119**, 8328-8337.
43. M. F. Vansco, H. Li and M. I. Lester, *J. Chem. Phys.*, 2017, **147**, 013907.
44. V. J. Esposito, T. Liu, G. Wang, A. Caracciolo, M. F. Vansco, B. Marchetti, T. N. V. Karsili and M. I. Lester, *J. Phys. Chem. A*, 2021, **125**, 6571-6579.
45. V. J. Esposito, O. Werba, S. A. Bush, B. Marchetti and T. N. V. Karsili, *Photochem. Photobiol.*, 2022, **98**, 763-772.
46. D. J. Bamford, L. E. Jusinski and W. K. Bischel, *Phys. Rev. A*, 1986, **34**, 185.
47. S. T. Pratt, P. M. Dehmer and J. L. Dehmer, *Phys. Rev. A*, 1991, **43**, 4702-4711.
48. A. Kramida, Ralchenko, Yu., Reader, J., NIST ASD Team, NIST Atomic Spectra Database <https://physics.nist.gov/asd>, (accessed August 22, 2022).
49. E. Antwi, R. E. Bush, B. Marchetti and T. N. V. Karsili, *Phys. Chem. Chem. Phys.*, 2022, **24**, 16724-16731.
50. C. A. Taatjes, O. Welz, A. J. Eskola, J. D. Savee, A. M. Scheer, D. E. Shallcross, B. Rotavera, E. P. F. Lee, J. M. Dyke, D. K. W. Mok, D. L. Osborn and C. J. Percival, *Science*, 2013, **340**, 177-180.
51. M. Nakajima and Y. Endo, *J. Chem. Phys.*, 2014, **140**, 011101.
52. H.-Y. Lin, Y.-H. Huang, X. Wang, J. M. Bowman, Y. Nishimura, H. A. Witek and Y.-P. Lee, *Nat. Commun.*, 2015, **6**, 7012.
53. H. Park, P. J. Miller, W. A. Chupka and S. D. Colson, *J. Chem. Phys.*, 1988, **89**, 6676-6686.
54. R. J. Yokelson, R. J. Lipert and W. A. Chupka, *J. Chem. Phys.*, 1992, **97**, 6153-6167.
55. G. A. Garcia, L. Nahon and I. Powis, *Rev. Sci. Instrum.*, 2004, **75**, 4989-4996.
56. W.-L. Ting, C.-H. Chang, Y.-F. Lee, H. Matsui, Y.-P. Lee and J. J.-M. Lin, *J. Chem. Phys.*, 2014, **141**, 104308.
57. K. S. Dooley, J. N. Geidosch and S. W. North, *Chem. Phys. Lett.*, 2008, **457**, 303-306.
58. M. J. Frisch, G. W. Trucks, H. B. Schlegel, G. E. Scuseria, M. A. Robb, J. R. Cheeseman, G. Scalmani, V. Barone, G. A. Petersson, H. Nakatsuji, X. Li, M. Caricato, A. V. Marenich, J. Bloino, B. G. Janesko, R. Gomperts, B. Mennucci, H. P. Hratchian, J. V. Ortiz, A. F. Izmaylov, J. L. Sonnenberg, D. Williams-Young, F. Ding, F. Lipparini, F. Egidi, J. Goings, B. Peng, A. Petrone, T. Henderson, D. Ranasinghe, V. G. Zakrzewski, J. Gao, N. Rega, G. Zheng, W. Liang, M. Hada, M. Ehara, K. Toyota, R. Fukuda, J. Hasegawa, M. Ishida, T. Nakajima, Y. Honda, O. Kitao, H. Nakai, T. Vreven, K. Throssell, J. J. A. Montgomery, J. E. Peralta, F. Ogliaro, M. J. Bearpark, J. J. Heyd, E. N. Brothers, K. N. Kudin, V. N. Staroverov, T. A. Keith, R. Kobayashi, J. Normand, K. Raghavachari, A. P. Rendell, J. C. Burant, S. S. Iyengar, J. Tomasi, M. Cossi, J. M. Millam, M. Klene, C. Adamo, R. Cammi, J. W. Ochterski, R. L. Martin, K. Morokuma, O. Farkas, J. B. Foresman and D. J. Fox, *Gaussian 16 Rev. A.03*, Gaussian Inc., Wallingford, CT.

59. V. P. Barber, S. Pandit, A. M. Green, N. Trongsiriwat, P. J. Walsh, S. J. Klippenstein and M. I. Lester, *J. Am. Chem. Soc.*, 2018, **140**, 10866-10880.
60. B. O. Roos, P. Linse, P. E. M. Siegbahn and M. R. A. Blomberg, *Chem. Phys.*, 1982, **66**, 197-207.
61. K. Andersson, P. Å. Malmqvist, B. O. Roos, A. J. Sadlej and K. Wolinski, *J. Chem. Phys.*, 1990, **94**, 5483-5488.
62. K. Andersson, P. Å. Malmqvist and B. O. Roos, *J. Chem. Phys.*, 1992, **96**, 1218-1226.
63. T. H. Dunning, *J. Chem. Phys.*, 1989, **90**, 1007-1023.
64. M. Barbatti, G. Granucci, M. Persico, M. Ruckebauer, M. Vazdar, M. Eckert-Maksić and H. Lischka, *J. Photochem. Photobiol. A*, 2007, **190**, 228-240.
65. M. Barbatti, M. Ruckebauer, F. Plasser, J. Pittner, G. Granucci, M. Persico and H. Lischka, *Wiley Interdiscip. Rev. Comput. Mol. Sci.*, 2014, **4**, 26-33.
66. L. Verlet, *Phys. Rev.*, 1967, **159**, 98.
67. J. C. Butcher, *J. ACM*, 1965, **12**, 124-135.
68. J. W. Park and T. Shiozaki, *J. Chem. Theory Comput.*, 2017, **13**, 2561-2570.
69. T. Shiozaki, *Wiley Interdiscip. Rev. Comput. Mol. Sci.*, 2018, **8**, e1331.
70. H.-J. Werner, P. J. Knowles, G. Knizia, F. R. Manby, M. Schütz, P. Celani, W. Györffy, D. Kats, T. Korona, R. Lindh, A. Mitrushenkov, G. Rauhut, K. R. Shamasundar, T. B. Adler, R. D. Amos, A. Bernhardsson, A. Berning, D. L. Cooper, M. J. O. Deegan, A. J. Dobbyn, F. Eckert, E. Goll, C. Hampel, A. Hesselmann, G. Hetzer, T. Hrenar, G. Jansen, C. Köppl, Y. Liu, A. W. Lloyd, R. A. Mata, A. J. May, S. J. McNicholas, W. Meyer, M. E. Mura, A. Nicklaß, D. P. O'Neill, P. Palmieri, D. Peng, K. Pflüger, R. Pitzer, M. Reiher, T. Shiozaki, H. Stoll, A. J. Stone, R. Tarroni, T. Thorsteinsson, M. Wang and M. Welborn *MOLPRO 2020.1, a package of ab initio programs*, see [www.molpro.net](http://www.molpro.net).
71. H.-J. Werner, P. J. Knowles, F. R. Manby, J. A. Black, K. Doll, A. Heßelmann, D. Kats, A. Köhn, T. Korona, D. A. Kreplin, Q. Ma, T. F. Miller, A. Mitrushchenkov, K. A. Peterson, I. Polyak, G. Rauhut and M. Sibaev, *J. Chem. Phys.*, 2020, **152**, 144107.
72. H.-J. Werner, P. J. Knowles, G. Knizia, F. R. Manby and M. Schütz, *Wiley Interdiscip. Rev. Comput. Mol. Sci.*, 2012, **2**, 242-253.
73. J. Towns, T. Cockerill, M. Dahan, I. Foster, K. Gaither, A. Grimshaw, V. Hazlewood, S. Lathrop, D. Lifka, G. D. Peterson, R. Roskies, J. R. Scott and N. Wilkens-Diehr, *Comput. Sci. Eng.*, 2014, **16**, 62-74.
74. T. N. V. Karsili, B. Marchetti, M. I. Lester and M. N. R. Ashfold, *Photochem. Photobiol.*, 2022, DOI: 10.1111/php.13665.
75. R. F. Borkman and D. R. Kearns, *J. Chem. Phys.*, 1966, **44**, 945-949.
76. D. Moule and K. Ng, *Can. J. Chem.*, 1985, **63**, 1378-1381.
77. S. Taylor, D. G. Wilden and J. Comer, *Chem. Phys.*, 1982, **70**, 291-298.
78. H. L. Huang, W. Chao and J. J. M. Lin, *Proc. Natl. Acad. Sci.*, 2015, **112**, 10857-10862.
79. B. J. Ratliff, C. C. Womack, X. N. Tang, W. M. Landau, L. J. Butler and D. E. Szpunar, *J. Phys. Chem. A*, 2010, **114**, 4934-4945.
80. Q. Zhong, L. Poth and A. W. Castleman, *J. Chem. Phys.*, 1998, **110**, 192-196.